

# Work Hardening, Dislocation Structure, and Load Partitioning in Lath Martensite Determined by *In Situ* Neutron Diffraction Line Profile Analysis



STEFANUS HARJO, TAKURO KAWASAKI, YO TOMOTA, WU GONG, KAZUYA AIZAWA, GEZA TICHY, ZENGMIN SHI, and TAMAS UNGÁR

A lath martensite steel containing 0.22 mass pct carbon was analyzed *in situ* during tensile deformation by high-resolution time-of-flight neutron diffraction to clarify the large work-hardening behavior at the beginning of plastic deformation. The diffraction peaks in plastically deformed states exhibit asymmetries as the reflection of redistributions of the stress and dislocation densities/arrangements in two lath packets: soft packet, where the dislocation glides are favorable, and hard packet, where they are unfavorable. The dislocation density was as high as  $10^{15} \text{ m}^{-2}$  in the as-heat-treated state. During tensile straining, the load and dislocation density became different between the two lath packets. The dislocation character and arrangement varied in the hard packet but hardly changed in the soft packet. In the hard packet, dislocations that were mainly screw-type in the as-heat-treated state became primarily edge-type and rearranged towards a dipole character related to constructing cell walls. The hard packet played an important role in the work hardening in martensite, which could be understood by considering the increase in dislocation density along with the change in dislocation arrangement.

DOI: 10.1007/s11661-017-4172-0

© The Minerals, Metals & Materials Society and ASM International 2017

## I. INTRODUCTION

LATH martensite steel is widely used in high-strength structural materials. It is obtained by quenching to room temperature (RT) from a temperature at which the austenitic phase is stable. The martensitic phase transformation produces a fine-grained structure with an extremely high dislocation density ( $>10^{15} \text{ m}^{-2}$ ).<sup>[1]</sup> The microstructure of lath martensite typically comprises

several packets with different crystallographic orientations in a prior austenite grain, where the packets are formed by several blocks.<sup>[2,3]</sup> The blocks are subdivided into sub-blocks with the same variant, and the smallest constituents are plate-like crystals called laths with sizes of several tens to several hundreds of nm.

The elastic limit of an as-quenched Fe-18Ni lath martensite steel is relatively low (300 MPa), and the tensile strength is 760 MPa at a nominal strain of approximately 1.5 pct.<sup>[4]</sup> This indicates a very high level of work hardening after yielding at the beginning of plastic deformation. Cold rolling was reported to increase the elastic limit substantially, resulting in higher 0.2 pct proof stress with increasing equivalent plastic strain.<sup>[4]</sup> To explain this deformation behavior, the changes in dislocation density ( $\rho$ ) in the cold-rolled and tensile-deformed lath martensitic Fe-18Ni alloys were measured by X-ray diffraction (XRD)<sup>[4]</sup> and neutron diffraction (ND)<sup>[5]</sup> based on the classical Williamson–Hall (W–H) plot.<sup>[6]</sup> The  $\rho$  values were found to decrease with plastic deformation, as evidenced by the decrease in the slopes of the classical W–H plots with plastic deformation.

In general, the change in flow stress ( $\Delta\sigma$ ) attributed to dislocations can be evaluated using Taylor's equation<sup>[7]</sup>:

$$\Delta\sigma = \sigma - \sigma_0 = \alpha\mu M_T b\sqrt{\rho}, \quad [1]$$

STEFANUS HARJO, TAKURO KAWASAKI, WU GONG, and KAZUYA AIZAWA are with the J-PARC Center, Japan Atomic Energy Agency 2-4 Shirane Shirakata, Tokai-mura, Naka-gun, Ibaraki, 319-1195, Japan. Contact e-mail: stefanus.harjo@j-parc.jp YO TOMOTA is with the Research Center for Structure Materials, National Institute for Materials Science, 1-2-1 Sengen, Tsukuba, Ibaraki 305-0047, Japan. GEZA TICHY is with the Department of Materials Physics, Eötvös University, P.O. Box 32, Budapest, 1518, Hungary. ZENGMIN SHI is with the College of Materials and Chemical Engineering, China Three Gorges University, 8 Daxue Rd, Xiling, Yichang, Hubei, China. TAMAS UNGÁR is with the Department of Materials Physics, Eötvös University and also with the Materials Performance Centre, The University of Manchester, M13 9PL, Manchester, UK.

Manuscript submitted December 15, 2016.

Article published online June 21, 2017

where  $\sigma$  is the flow stress attributed to dislocations,  $\sigma_0$  is the sum of the friction stress of dislocations and the stress attributable to the effect of solute element strengthening,  $\alpha$  is a geometric coefficient between zero and unity,  $\mu$  is the shear modulus,  $M_T$  is the Taylor factor, which accounts for the effect of texture, and  $b$  is the Burgers vector.

The value of  $\alpha$  is usually assumed to be unchanged during deformation; hence, the increase in  $\Delta\sigma$  is caused solely by the increase in  $\rho$ , unless the grain size is very small. Therefore, the decrease in  $\rho$  for lath martensitic Fe-18Ni alloy, as reported in References 4 and 5, is puzzling. The results of  $\rho$  reported in References 4 and 5 remain questionable despite the fact that the large  $\rho$  value invoked by martensitic transformation can decrease slightly as a result of plastic deformation, as reported in Reference 8. Hutchingson *et al.*<sup>[9]</sup> carried out similar experiments but interpreted the slopes of the classical W–H plots to indicate residual intragranular shear stresses generated during martensitic transformation. They claimed that the residual intragranular shear stresses were reduced in magnitude by plastic deformation, subsequently controlling the stress–strain behavior. However, their interpretation is questionable when considering the diffraction profile analysis presented in this paper.

*In situ* ND is a powerful tool for clarifying phenomena in various engineering applications.<sup>[10–17]</sup> We have reported *in situ* high-resolution ND experiments of a lath martensite steel containing 0.22 mass pct carbon during tensile deformation.<sup>[17]</sup> We found that the initial homogeneous lath structure was disrupted by plastic tensile deformation, producing a composite on the length scale of martensite lath packets. The diffraction profiles of plastically strained martensite steel revealed to be characteristically asymmetric as observed in materials with heterogeneous dislocation structures.<sup>[18,19]</sup> The diffraction patterns were evaluated by the convolutional multiple whole profile (CMWP) procedure based on physically modeled profile functions for dislocations, crystallite size, and planar defects.<sup>[20,21]</sup> The lath packets oriented favorably for dislocation glide became soft (soft-packet orientation components, SO), and those unfavorably for dislocation glide became hard (hard-packet orientation components, HO), causing dislocation density to become smaller and larger compared to the initial average dislocation density, respectively. The decomposition into SO and HO was accompanied by load redistribution and the formation of long-range internal stress between the two lath packets.

In the present work, which is the second part of Reference 17, the evolution of dislocation properties and lattice strain during tensile deformation is discussed in terms of the composite behavior of the lath-packet structure. The average dislocation densities provided by neutron line profile analysis are compared with scanning transmission electron microscopy (STEM) observations. The changes in dislocation character and dislocation arrangement during tensile deformation in the two types of lath packets are discussed in relation to work hardening. The work-hardening mechanism of the lath

martensite is further discussed by correlating the dislocation structure with the flow stress in Taylor's equation.

## II. EXPERIMENTAL

The sample used in this study was a lath martensite steel with the chemical composition of Fe-0.22C-0.87-Si-1.64Mn-0.024Ti-0.0015B-0.0025N (mass pct).<sup>[22]</sup> Specimens were prepared from a 20-mm-thick plate that was austenitized at 1173 K (900 °C) for 3.6 ks, quenched, and then tempered at 453 K ranging to 473 K (180 °C to 200 °C) for approximately 10.8 ks. The average packet and block sizes were 20 and 4  $\mu\text{m}$ , respectively. A rod-shaped specimen with a diameter of 5 mm and a length of 15 mm was prepared for *in situ* ND experiments during tensile testing using TAKUMI,<sup>[23]</sup> a high-resolution time-of-flight (TOF) neutron diffractometer for engineering materials sciences at the Materials and Life Science Experimental Facility of the Japan Proton Accelerator Research Complex.

Tensile deformation for *in situ* ND was performed in a stepwise manner with load control in the elastic region, whereas in a continuous manner in the plastic region. The crosshead speed was constant (the strain rate was  $10^{-5} \text{ s}^{-1}$ ) in the plastic region. The strain was monitored by a strain gage glued to the specimen. The deformation in the plastic region was increased stepwise to arbitrary strains followed by unloading. The ND data were collected continuously using an event-recording mode during tensile deformation. Further details regarding the ND conditions are given in our previous paper.<sup>[17]</sup> The diffraction patterns related to the step load-holding states, plastic deformations, and unloaded states after plastic deformation were then extracted according to the macroscopic stress and strain data. The macroscopic stress and strain values relevant to the diffraction patterns were averaged over the interval times for data extraction. Figure 1 shows the macroscopic stress–strain curve of the specimen. The elastic limit was approximately 350 MPa; therefore, the rate of work hardening was extremely high. In the macroscopic stress–strain curve obtained from continuous loading under the same strain rate until fracture, a very high tensile strength of approximately 1.65 GPa and a uniform strain of approximately 6.1 pct were confirmed.

Data analyses for evaluating the lattice constant, phase fraction, and lattice strain were performed using Z-Rietveld software,<sup>[24]</sup> while dislocations were analyzed using the CMWP procedure. The diffraction profiles of  $\text{LaB}_6$  powder measured under the same conditions as the *in situ* ND measurements were used to determine the instrumental peak profiles for the dislocation analyses. Figure 2 shows the observed and Rietveld-calculated or CMWP-fitted ND patterns before tensile deformation. During the Rietveld or CMWP fitting, the second phase of  $\gamma$  was also analyzed to exclude its influence on the results of the main phase of martensite. The data analyses using Z-Rietveld were conducted for all diffraction patterns, whereas the dislocation analyses using the CMWP procedure were performed only on the diffraction profiles collected in the unloaded states after plastic deformation.

STEM observations were performed using an electron microscope (Tecnai G2F20) with bright field (BF) and annular dark field (ADF) modes operated at 200 kV. The thickness of the observation area in the STEM foil was estimated using electron energy loss spectroscopy,<sup>[25]</sup> and the  $\rho$  value was determined using the linear cross-sectioning method.

### III. RESULTS AND DISCUSSION

#### A. Crystal Structure and Phase Fraction

The crystal structure used in the Rietveld analysis (Figure 2(a)) for martensite was BCC. The crystal

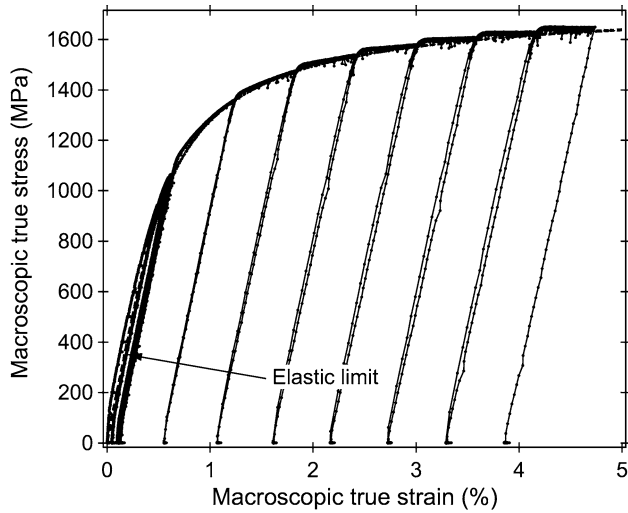


Fig. 1—Macroscopic stress–strain curve of the lath martensite steel in this study.

structures of lath martensite steels with carbon contents below 0.6 mass pct were reported to be BCC at RT.<sup>[26]</sup> Although martensite in a Fe-30Ni-0.2C alloy was reported to have a BCT structure with a  $c/a$  ratio of approximately 1.02,<sup>[27]</sup> the sample used in this study was Ni-free, and the martensite peaks in Figure 2(a) were perfectly fitted using the TAKUMI instrumental profile shape function with a BCC structure. A random texture was found in the as-heat-treated state (before tensile deformation) from the ratio of  $hkl$  peak integrated intensity. A weak  $\alpha$ -fiber texture was developed after 4.7 pct tensile deformation.

Retained austenite ( $\gamma$ ) was confirmed in the specimen, as shown in Figure 2(a), and its fraction before tensile deformation was refined to be approximately 3.7 pct. The lattice constants of martensite and  $\gamma$  were determined to be 0.28646(0) nm and 0.35912(3) nm, respectively. Figure 3 shows the fractions of  $\gamma$  measured in the unloaded states after plastic tensile deformation. The  $\gamma$  phase still existed after 4.7 pct tensile deformation, but its fraction decreased to approximately 2.2 pct. A small amount of  $\gamma$  might transform to martensite during plastic tensile deformation. The existence of  $\gamma$  was difficult to confirm in the microscopy images, likely because of its very small size and/or martensitic transformation during specimen preparation.

#### B. Strain Anisotropy and Elastic Anisotropy

The  $hkl$ -dependent Young's moduli ( $E_{hkl}$ ) values for martensite obtained from the lattice strain results are summarized in Table I. The Young's moduli values in a cubic crystal must follow the following linear relation<sup>[28]</sup>:

$$1/E_{hkl} = B + FH^2, \quad [2]$$

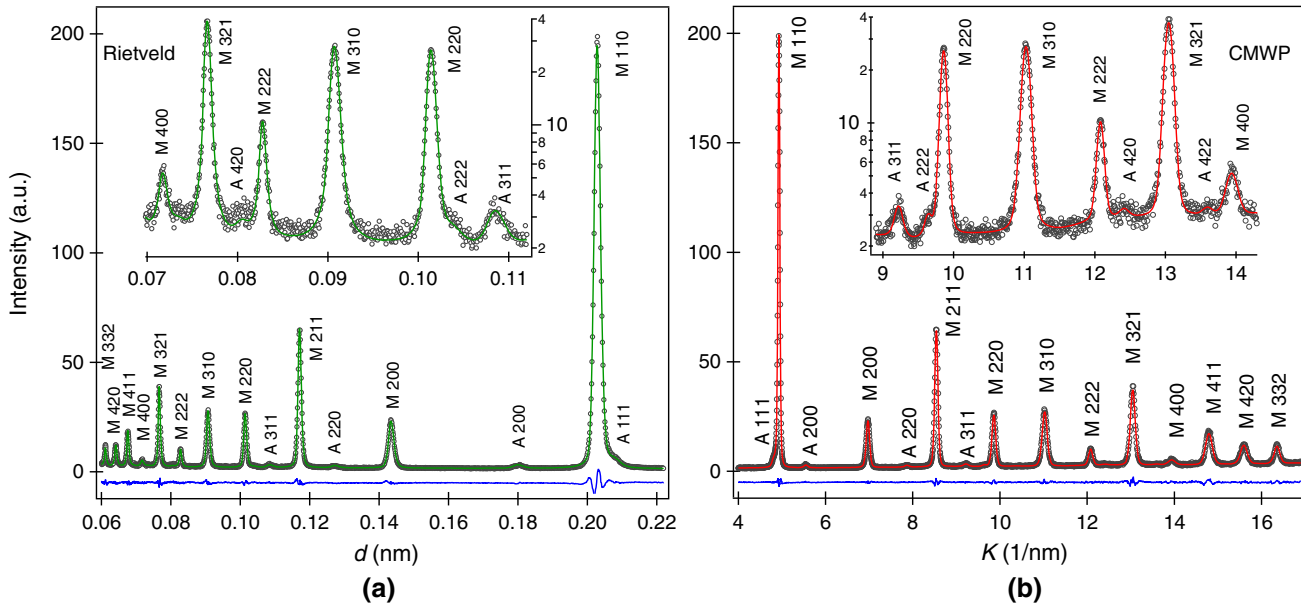


Fig. 2—The observed (black circles) and Rietveld-fitted [green line in (a)] or CMWP-fitted [red line in (b)] ND patterns before tensile deformation.  $K = 1/d$ , where  $d$  is the lattice spacing. The blue line is the residual between the fitted and observed profiles. The embedded figure in (a) or (b) shows the enlarged pattern with log scale on the vertical axis for the high-index peak range. M and A indicate martensite and retained austenite, respectively (color for online only).

where  $B$  and  $F$  are constants, and  $H^2$  is the fourth order invariant of  $hkl$ ,  $H^2 = (h^2k^2 + h^2l^2 + k^2l^2) / (h^2 + k^2 + l^2)^2$ . The inverses of the measured  $E_{hkl}$  values are plotted vs  $H^2$  in Figure 4, indicating that Eq. [2] was fulfilled perfectly within the experimental errors with  $B = 0.0059$  and  $F = -0.0062$ .  $B$  and  $F$  are related to the elastic constants ( $c_{11}$ ,  $c_{12}$ , and  $c_{44}$ ) as follows [28]:

$$B = \frac{c_{11} + c_{12}}{(c_{11} + 2c_{12})(c_{11} - c_{12})} \text{ and } F = \frac{1}{c_{44}} - \frac{2}{c_{11} - c_{12}}. \quad [3]$$

$B$  and  $F$  are clearly insufficient to provide three elastic constants without any further information. Fortunately, we know that the  $c_{44}/c_{12}$  ratio for metals is usually between 0.5 and 0.7.[29] Taking  $c_{44}/c_{12} = 0.6$ , using Eq. [3], the values of  $B$  and  $F$  provide the elastic constants for the martensite investigated here:

$$c_{11} = 283(5) \text{ GPa}, c_{12} = 161(4) \text{ GPa}, \text{ and } c_{44} = 97(4) \text{ GPa}. \quad [4]$$

With these elastic constants, the elastic anisotropy ( $A$ ) of our martensite material was determined to be 1.59. The  $A$  value of  $\alpha$ -Fe is 2.4.[30] The  $A$  value of a martensite steel investigated in Reference 30 was 1.01. However, the compositions of the martensite investigated here and that reported in Reference 30 are different. The composition of the present martensite steel is Fe-0.22C-0.87Si-1.64Mn-0.024Ti (mass pct), whereas the composition of the steel reported in Reference 30 is Fe-0.52C-0.22Si-1.0Mn-0.3Al (mass pct). The  $A$  value of 1.59 is between the values of  $\alpha$ -Fe and the martensite steel in Reference 30. This indicates

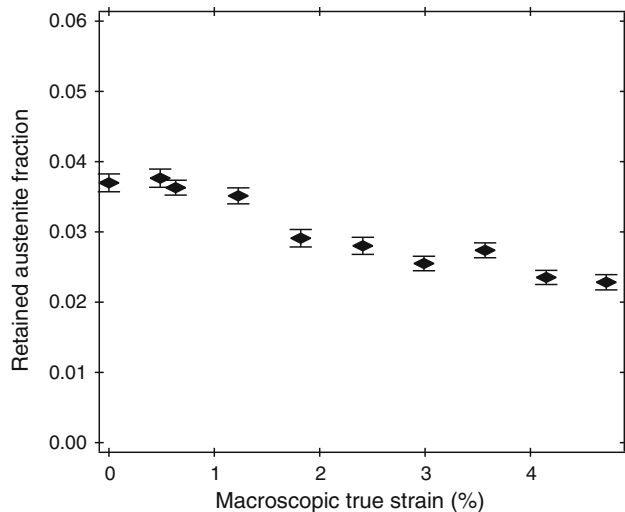


Fig. 3—Fractions of retained austenite measured after plastic tensile deformation in the unloaded states.

that the elastic anisotropy is rather sensitive to the composition and probably the exact quenching conditions of martensitic steel.

Strain anisotropy line broadening means that the full width at half maximum (FWHM) values of the diffraction peaks are not a monotonic function of diffraction order.[31] Figure 5(a) shows the FWHM values of martensite steel before deformation and with 0.6, 3, and 4.7 pct tensile deformation vs  $K = 1/d$ , where  $d$  is the lattice spacing. The FWHM values were evaluated by a Gaussian function from the physical profiles of the diffraction peaks that are free from instrumental effects, as provided by the CMWP procedure. The increase in FWHM with  $K$  indicates substantial microstrain caused by the large dislocation density. The apparent scatter of the FWHM values around the global ascending trend is typical for strain anisotropy. Strain anisotropy can be rectified by accounting for the  $hkl$ -dependent dislocation contrast  $C(hkl)$ . [31] In polycrystalline cubic materials,  $C(hkl)$  can be averaged over the permutations of  $hkl$  and written as [32]

$$\bar{C} = \bar{C}_{h00}(1 - qH^2), \quad [5]$$

where  $\bar{C}_{h00}$  is the average contrast for  $h00$ -type reflections, and  $q$  is a parameter that depends on the dislocation character (*e.g.*, screw- or edge-type) and the elastic anisotropy of the material. In References 31 and 33, the apparently irregular behavior of the FWHM values in the conventional W–H plot was rectified when  $K$  was replaced by  $K\sqrt{\bar{C}}$  in the modified W–H plot. The irregular behavior of the FWHM values in Figure 5(a) was rectified when  $q$  was 1.7, as shown in Figure 5(b). According to the theoretical computation for BCC with a slip system of  $\langle 111 \rangle \{110\}$ ,  $A = 1.6$ , and  $c_{44}/c_{12} = 0.6$ ,  $q$  values of 0.2 and 2.5 correspond to edge-type and screw-type dislocations, respectively.[33] Therefore, the  $q$  value of 1.7 in Figure 5(b) indicates that the dislocations have a mixed edge and screw character with screw-type being dominant. Figure 5(b) shows that the FWHM values follow a perfect straight line, confirming the evaluation of the elastic constants and the  $q$  value of 1.7. According to a TEM study,[34] a dislocated martensite structure consists of two kinds of dislocations: straight screw-type dislocations induced by lattice invariant shear and tangled dislocations generated in the austenite matrix to relax the internal stress caused by transformation strain. The tangled dislocations are inherited in martensite. This TEM work supports the obtained  $q$  value along with the mixture of screw- and edge-type dislocations in as-quenched martensite.

The slopes of the straight lines in Figure 5(b) decrease slightly with increasing macroscopic strain. It is important to note here that the profile does contain the width part and the tail part. The tail is however ignored in the FWHM value. The decrease in FWHM was also

Table I. The Values of  $hkl$ -Dependent Young's Moduli ( $E_{hkl}$ )

| $hkl$     | 110    | 200    | 211    | 220    | 310    | 222    |
|-----------|--------|--------|--------|--------|--------|--------|
| $E_{hkl}$ | 233(1) | 167(2) | 233(2) | 229(3) | 183(3) | 250(8) |



accompanied by changes in peak shape from Gaussian to Lorentzian. This peak shape change might be associated with the change in dislocation arrangement. The dislocation densities, characteristics, and arrangements evaluated by analyzing the whole profile using the CMWP procedure will be discussed in detail in the next sections.

### C. Dislocation Densities Based on CMWP Analysis Assuming Symmetrical Peak Profiles and STEM Observation

In this section, we first explain the results of the CMWP analysis under the assumption that a

symmetrical peak profile was maintained throughout tensile deformation, although we reported that the symmetrical diffraction profiles before tensile deformation became asymmetric as a result of plastic strain.<sup>[17]</sup> This analysis was performed to obtain average dislocation densities and compare them with the dislocation densities based on STEM observations and the CMWP analysis considering peak asymmetry (described later).

The average values of  $\rho$  ( $\rho_{ave}$ ) in the axial direction are summarized in Figure 6. The parameters are labeled as averages here to express the results from all packets regardless of the presence of SO and HO. The value of  $\rho_{ave}$  before tensile deformation was already high (approximately  $4.0 \times 10^{15} \text{ m}^{-2}$ ). This value is consistent with that reported for a lath martensite steel with a similar carbon content (0.18 mass pct) determined using TEM.<sup>[35]</sup> This high value is attributed to martensitic transformation, which is difficult to achieve by plastic tensile deformation. The value of  $\rho_{ave}$  changed slightly with increasing macroscopic strain, although an increase in flow stress was observed. These  $\rho_{ave}$  values lie on the same experimental curves as those obtained in cold-rolled lath martensite steel plates when they were replotted as a function of the equivalent plastic strain.

TEM observations were used to confirm the change in dislocation density, although the CMWP fitting of TOF ND profiles was already demonstrated to be reliable.<sup>[36]</sup> Figure 7(a) shows the STEM-BF and STEM-ADF images obtained from a specimen before tensile deformation, and Figure 7(b) shows the images after 4.7 pct tensile deformation. The dislocation densities were determined using five ADF images: three images with the incident beam parallel to  $\langle 111 \rangle$  and two images with the incident beam parallel to  $\langle 001 \rangle$  (all  $a/3 \langle 111 \rangle$ -type dislocations were visible under these incident beam conditions). The  $\rho_{ave}$  value before tensile deformation

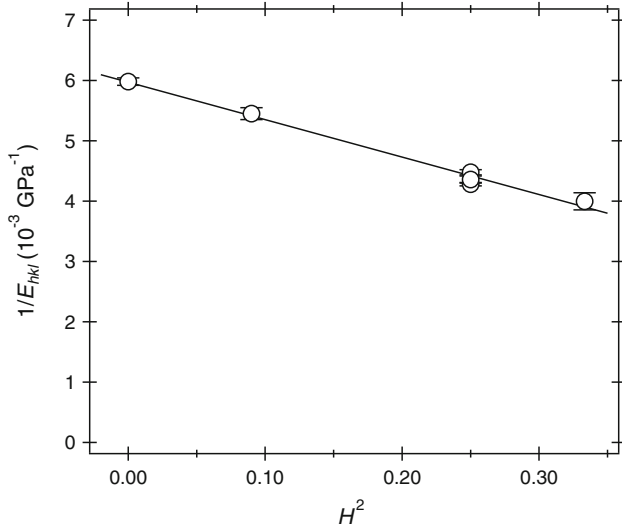


Fig. 4—Measured  $1/E_{hkl}$  values vs  $H^2$ .

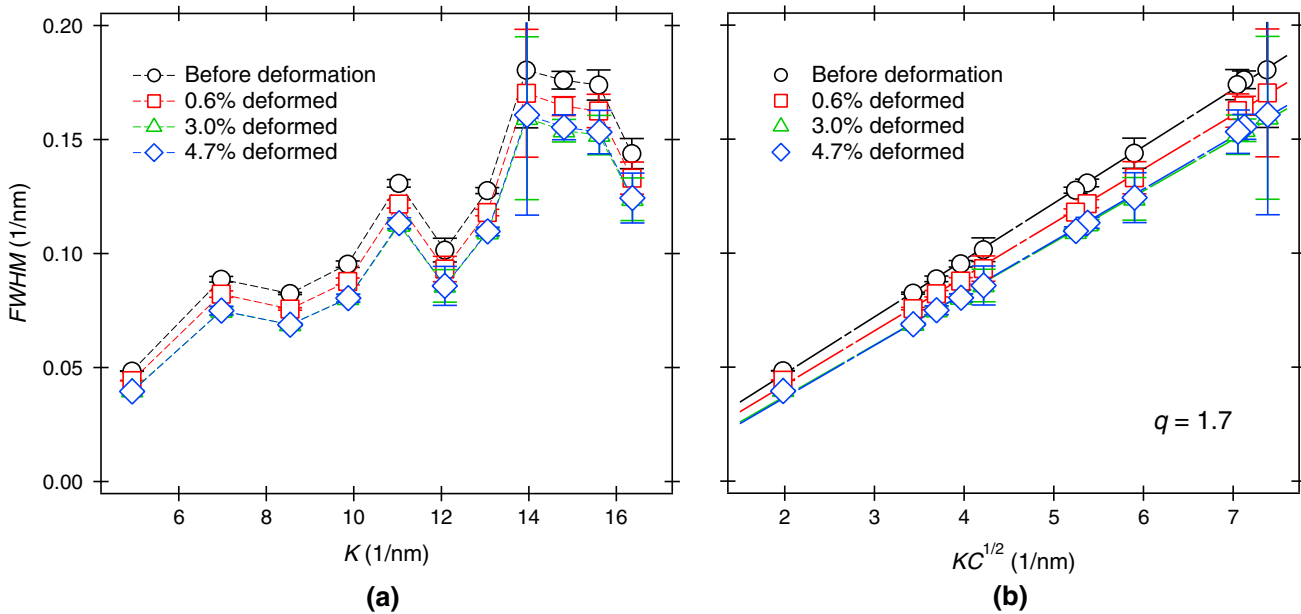


Fig. 5—(a) FWHM values of the physical profiles free from instrumental effects (as provided by CMWP analysis) vs  $K = 1/d$  for martensite steel before deformation and at after 0.6, 3, and 4.7 pct tensile deformation. (b) The same FWHM values as in (a) vs  $K\sqrt{C}$  in the modified W–H plot with  $q = 1.7$  (color for online only).

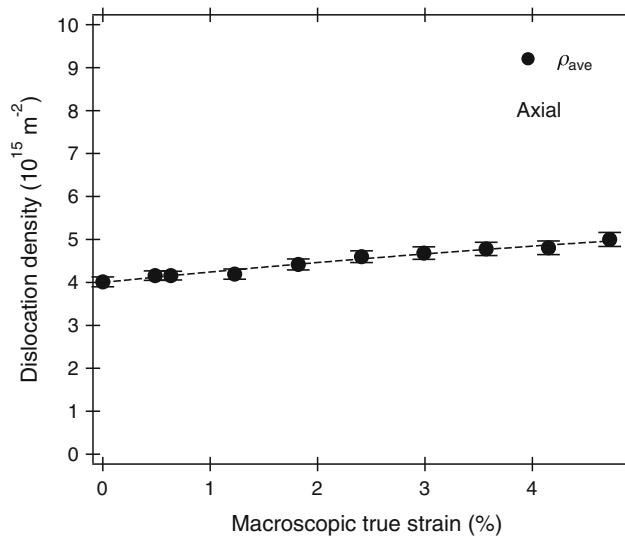


Fig. 6—Dislocation densities obtained from CMWP fitting assuming a symmetrical peak profile in the axial direction.

was determined to be between  $8.79 \times 10^{14}$  and  $1.48 \times 10^{15} \text{ m}^{-2}$  (average =  $1.17 \times 10^{15} \text{ m}^{-2}$ ), which was quite close to the TEM-based value reported by Morito *et al.*<sup>[35]</sup> for a lath martensite steel with a similar carbon concentration (average =  $1.11 \times 10^{15} \text{ m}^{-2}$  in an Fe-0.18C steel). Meanwhile, the  $\rho_{\text{ave}}$  value after 4.7 pct tensile deformation was determined to be between  $9.05 \times 10^{14}$  and  $1.45 \times 10^{15} \text{ m}^{-2}$  (average =  $1.18 \times 10^{15} \text{ m}^{-2}$ ), indicating no significant difference between the two conditions. These values are smaller than those determined by the CMWP method using the ND profiles presented in Figure 6. The dislocation densities determined by TEM are lower than those determined by diffraction methods in many cases. In our case, this is because the present TEM observations mainly counted dislocations located inside of lathes, whereas the CMWP method evaluated all dislocations, including those at the sub-boundaries. Huang *et al.*<sup>[37]</sup> reported that the total dislocation density in lath martensite of an interstitial free steel containing Mn and B is the sum of the dislocations in sub-block boundaries ( $2 \times 10^{14} \text{ m}^{-2}$ ), in lath boundaries ( $3 \times 10^{14} \text{ m}^{-2}$ ; they are called dislocation boundaries in Reference 37), and in the volume between boundaries ( $3 \times 10^{14} \text{ m}^{-2}$ ). They evaluated dislocation boundaries using the misorientation angle of the sub-block or lath boundary and the boundary area per unit area of sub-block or lath. Because the steel used in the present study contained 0.22 mass pct carbon, the dislocation boundaries must be higher than those reported by Huang *et al.*<sup>[37]</sup> Hence, the total dislocation density can be roughly estimated to be three times higher than that inside of laths. In conclusion, the results confirm that the change in  $\rho_{\text{ave}}$  during tensile deformation was small and did not exhibit a decreasing trend. The decreasing  $\rho$  value with deformation progress determined using the classical W–H plot based on peak width reported in References 4 and 5 might be erroneous because the entire peak shape (including the tail part) was not taken into account in the analysis.

#### D. Dislocation Density and Dislocation Character Obtained by CMWP Analysis with Dual-Packet Contribution

As described in our previous paper,<sup>[17]</sup> the diffraction profiles of plastically strained martensite steel revealed to be characteristically asymmetric. We have proposed a fitting procedure to analyze the ND patterns in the unloaded states after plastic tensile deformation using a dual-packet contribution composed of two BCC structures in the CMWP analyses. The details are described in Reference 17. This fitting procedure was supported by a crystallographic relationship in low carbon martensite [*i.e.*, the prior austenite (111) plane is parallel to the martensite (110) plane, and the habit plane of lath martensite is nearly (110)].<sup>[2,3]</sup> For example, the orientation difference in the diffracted (110) plane with respect to the lath boundary [another (110)] is either 60 or 90 deg, and in the diffracted (200) plane, 45 or 90 deg. However, these analyses could not be performed for the ND patterns taken during loading because the statistical accuracy of the data was insufficient. The fraction of HO ( $f_{\text{HO}}$ ) was found to be approximately 50 pct and was unchanged during tensile deformation.

Figure 8(a) shows the dislocation densities in the packet components ( $\rho_{\text{HO}}$  for HO and  $\rho_{\text{SO}}$  for SO) obtained from the CMWP fitting assuming dual-packet contribution. The  $\rho_{\text{HO}}$  value increased with increasing macroscopic strain up to the order of  $10^{16} \text{ m}^{-2}$ , whereas the  $\rho_{\text{SO}}$  value decreased rapidly at the beginning of deformation to the order of  $10^{14} \text{ m}^{-2}$  and then hardly changed. Further details regarding  $\rho_{\text{HO}}$  and  $\rho_{\text{SO}}$  are reported in our previous paper.<sup>[17]</sup> The total average dislocation density ( $\rho_{\text{t}}$ ) calculated from the  $\rho_{\text{HO}}$  and  $\rho_{\text{SO}}$  values as the weighted average according  $\rho_{\text{t}} = f_{\text{HO}} \rho_{\text{HO}} + (1 - f_{\text{HO}}) \rho_{\text{SO}}$  showed a similar tendency as the  $\rho_{\text{ave}}$  value shown in Figure 6 but with slightly larger values. It is important to note here that the  $\rho_{\text{ave}}$  values in Figure 6 were obtained by the CMWP procedure assuming a symmetrical profile, whereas  $\rho_{\text{HO}}$  and  $\rho_{\text{SO}}$  were provided by allowing the existence of two different packet populations. Using this procedure, the asymmetries in the peak profiles were correctly taken into account, and the obtained results are considered to be physically correct.

Figure 8(b) shows the values of  $q$  for HO and SO ( $q_{\text{HO}}$  and  $q_{\text{SO}}$ , respectively). The  $q$  value obtained before tensile deformation was approximately 1.7, indicating that before tensile deformation, the dislocations were of mixed edge- and screw-type with a larger proportion of screw-type dislocations. Screw-type dislocations are mainly found in BCC polycrystalline materials.<sup>[33,38]</sup> The  $q_{\text{SO}}$  values were almost unchanged with deformation from the state before tensile deformation, indicating that dislocations with screw character were dominant in the SO. In contrast, the  $q_{\text{HO}}$  value decreased largely at the beginning of tensile deformation to be approximately 0.6, indicating that the proportion of edge dislocations increased in the HO. These results support the simulation results reported in our previous paper (Table I in Reference 17). Screw dislocations can move in any direction and therefore are annihilated relatively

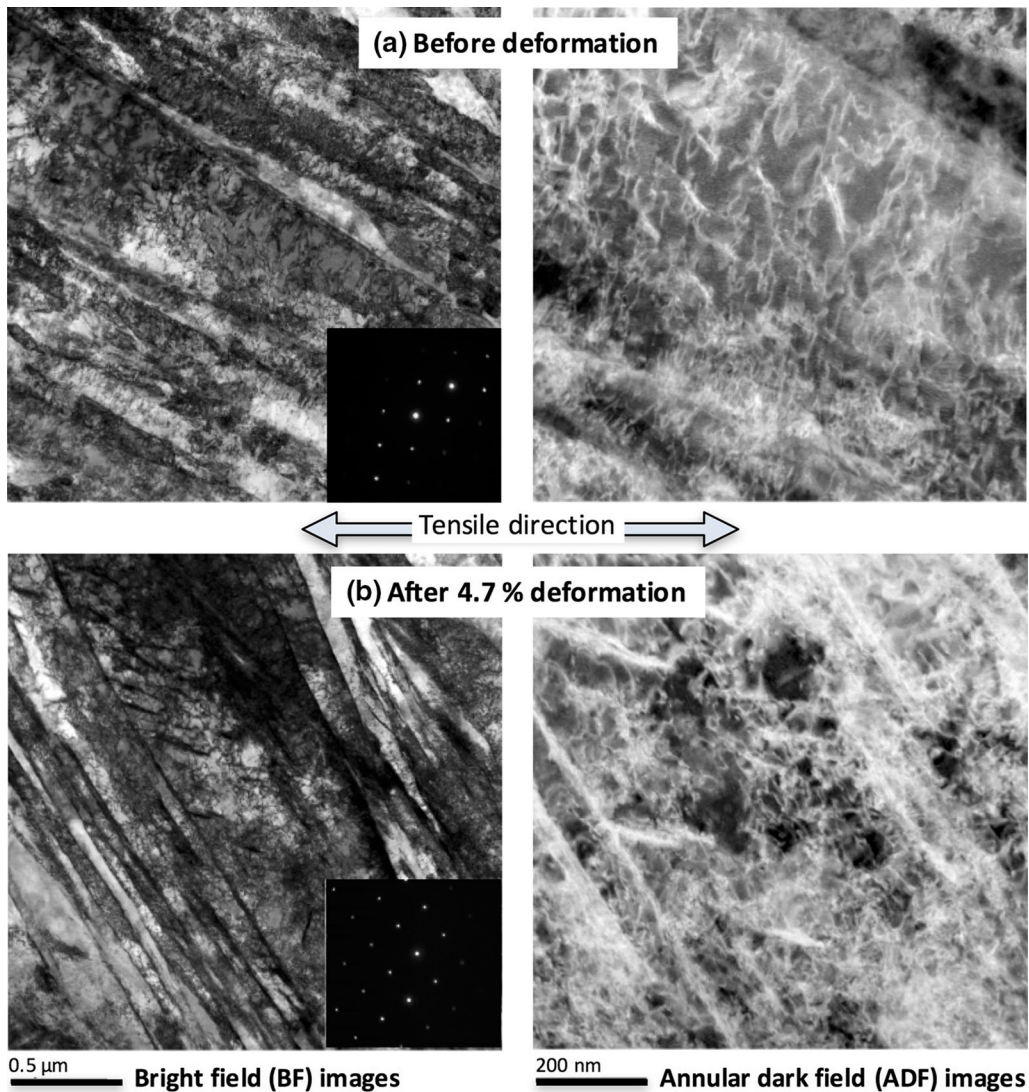


Fig. 7—STEM images (a) before tensile deformation and (b) after 4.7 pct tensile deformation. The incident beam was parallel to the (001) orientation.

easily, even when they are far apart from each other.<sup>[39]</sup> Edge dislocations must either glide on slip planes or climb to be annihilated and therefore are only annihilated within short distances.<sup>[39]</sup>

The relatively unchanged  $q$  value of 1.7 and the decreasing dislocation density during deformation in the SO are consistent with the results of the modified W–H plot, as described in Section III–B, in which good linearity was maintained with  $q = 1.7$ , and the slopes decreased slightly with increasing macroscopic strain. Therefore, the FWHM values of the profiles are mainly of the profile parts of the SO. As shown in our previous paper (Figures 5(c) and (d) in Reference 17), the total physical diffraction profiles in the plastically tensile-deformed martensite consisted of two peaks. The peak with larger intensity and smaller FWHM corresponded to the SO, whereas the other peak with smaller intensity and larger FWHM corresponded to the HO. The FWHM values shown in Figure 5 clearly correspond

to the peaks with larger intensity, for which the FWHM values decreased slightly with strain.

#### E. Dislocation Arrangement and Crystallite Size Based on CMWP Analysis

The parameter  $M$ , which is the product of the effective cutoff radius of dislocation ( $Re$ ) and the square root of  $\rho$  ( $M = Re\sqrt{\rho}$ ), indicates the dislocation arrangement.<sup>[20]</sup> A small or large value of  $M$  indicates that the dipole character and the screening of the displacement field of dislocations are strong or weak, respectively.

Figure 9 shows the average values of  $M$  ( $M_{ave}$ ) obtained from CMWP fitting assuming a symmetrical peak profile and  $M$  value corresponding to the HO ( $M_{HO}$ ) obtained from the CMWP fitting assuming multi-packet contribution. The values of  $M_{ave}$  and  $M_{HO}$  were large before tensile deformation. They decreased rapidly at the beginning of deformation and

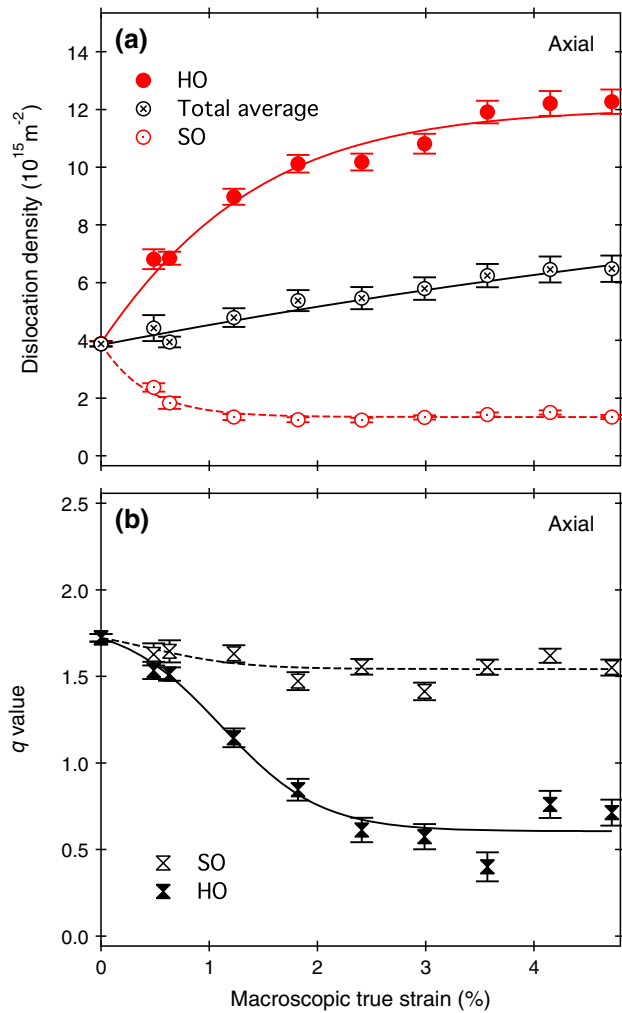


Fig. 8—(a) Dislocation density and (b) parameter depending on the dislocation character ( $q$ ) in the HO or SO obtained from CMWP fitting assuming multi-packet contribution in the axial direction (color for online only).

then gradually decreased with the progress of tensile deformation, finally becoming less than 1.0. Meanwhile, the values of  $M$  for SO ( $M_{\text{SO}}$ ) remained large during tensile deformation. The large values of  $M_{\text{SO}}$  suggest that it has little effect on dislocation density, which can be attributed to the balanced competition of dislocation generation and annihilation, resulting in small work softening. The values of  $M_{\text{ave}}$  were consistent with those of  $M_{\text{HO}}$  within the analytical error. Therefore, the profile shapes corresponding to  $Re$  or  $M$  can be concluded to mainly be the profile parts of the HO. The decrease in  $M_{\text{HO}}$  indicates that the dislocations in the HO rearranged towards a configuration with a stronger dipole character of dislocation. A similar tendency for  $M$  with respect to the reduction in thickness was also observed by XRD in a carbon-free Fe-18Ni alloy after cold rolling.<sup>[40]</sup> These results suggest that the interactions between dislocations and solute carbon atoms do not affect the re-arrangement of dislocations during RT deformation.

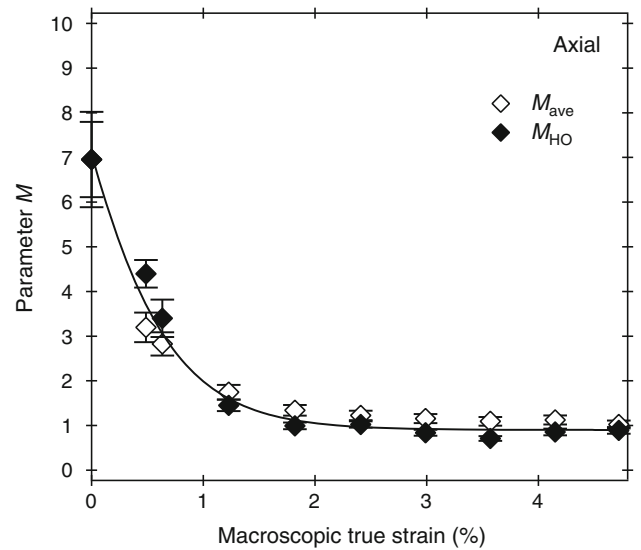


Fig. 9—Average arrangement parameter  $M$  obtained from CMWP fitting assuming a symmetrical peak profile and parameter  $M$  in the HO obtained from CMWP fitting assuming multi-packet contribution in the axial direction.

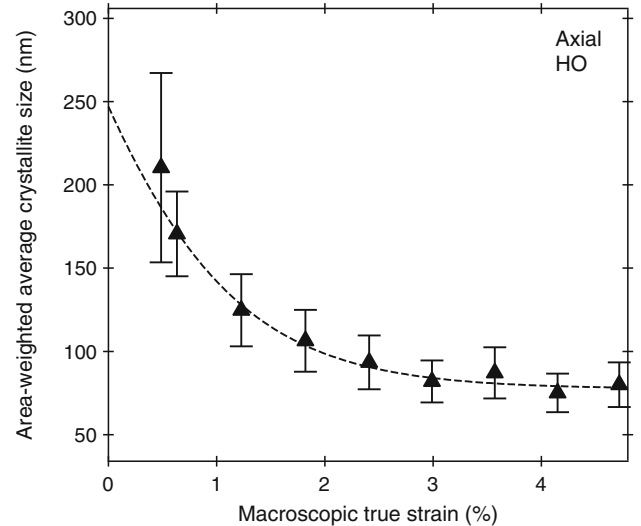


Fig. 10—Area-weighted average crystallite size (subgrain size) in the HO.

Figure 10 shows the area-weighted average crystallite size, which is relevant to the subgrain size in the HO in the present case. The subgrain size decreased with increasing macroscopic strain. TEM studies indicated that the lath martensite structure changes to a deformation cell structure with plastic deformation.<sup>[4,40–42]</sup> The lath boundaries became difficult to be distinguish and changed to cell structures with dense dislocation walls after cold rolling. These findings indicate that the dislocation cell boundaries increased, while the subgrain size decreased. Therefore, the results in Figure 10 are in good agreement with these previous TEM works. The decreasing trend in the subgrain size in the HO (Figure 10) is similar to the decreasing trend in  $M_{\text{HO}}$



shown in Figure 9. Therefore, the decrease in  $M_{HO}$  indicates that two effects (*i.e.*, increasing dipole character of the dislocation structure and decreasing subgrain size related to the formation of dislocation cells) acted simultaneously. Decreasing trends in both  $M$  and crystallite size were also observed by Stráská *et al.*<sup>[43]</sup> in a magnesium alloy processed by high-pressure torsion.

### F. Lattice Strain

First, all ND patterns were fitted using Z-Rietveld assuming a symmetrical peak profile to determine the average lattice constants and peak positions. The lattice strain can be evaluated from the peak shift according to the following equation:

$$\varepsilon^{hkl} = (d^{hkl} - d_0^{hkl}) / d_0^{hkl}, \quad [6]$$

where  $\varepsilon$ ,  $d$ , and  $d_0$  are the lattice strain, measured lattice spacing, and reference lattice spacing, respectively. The lattice spacing determined before tensile deformation was used as  $d_0$ . Figure 11 shows the lattice strains in the axial direction measured for martensite and  $\gamma$ . In Figure 11(a), all martensite- $hkl$  lattice strain responses to the macroscopic stress deviated from linearity to have smaller rates of increase. In contrast, the  $\gamma$   $\langle 311 \rangle$  lattice strains had larger values than the martensite lattice strains at the related macroscopic stresses. Note that the  $\langle 311 \rangle$  lattice strain represents the bulky elastic strain for FCC polycrystalline materials.<sup>[10,15]</sup> In Figure 11(b), the average residual lattice strain in the unloaded state after plastic tensile deformation for martensite that was averaged over  $\langle hkl \rangle$  decreased and became compressive with increasing macroscopic strain, whereas that for  $\gamma$

increased in the opposite tensile direction. These results indicate that  $\gamma$  plays the role of the hard phase in the material used in this study. Similar behaviors have been observed in transformation-induced plasticity-aided multiphase steels.<sup>[12,14]</sup> In these steels, retained austenites show higher flow stress than the ferrite-bainite matrix because of carbon enrichment. This effect was not observed in the lath martensite steel used in this study because carbon enrichment was minor. Similar behavior was observed in Fe-Cu alloy,<sup>[16]</sup> in which tiny copper precipitates behaved as the hard phase despite the low flow stress at the elasto-plastic deformation in copper polycrystalline aggregates.<sup>[13]</sup> Extremely small austenite particles embedded in the strong martensite matrix have been speculated to exhibit high flow resistance similar to the tiny Cu particles in iron. However, the martensite lattice strains are still maintained in the increasing tendency with increasing macroscopic stress, indicating work hardening.

Next, the ND patterns of the unloaded states after plastic tensile deformation were analyzed to determine the peak positions of the SO and HO based on a dual-packet contribution composed of two BCC structures in both the Z-Rietveld and CMWP analyses. Figure 12 shows the fits obtained using Z-Rietveld. The fit was improved by using two sub-peaks corresponding to contributions from SO and HO. The SO sub-peak had a higher intensity and smaller FWHM value, while the HO sub-peak had a lower intensity and larger FWHM value.

Residual strains operating in the two components of lath martensite, SO and HO, were computed using a composite model assuming zero stress balance. In fact, the balances of residual strains in the SO and the HO are the average residual lattice strains for martensite shown

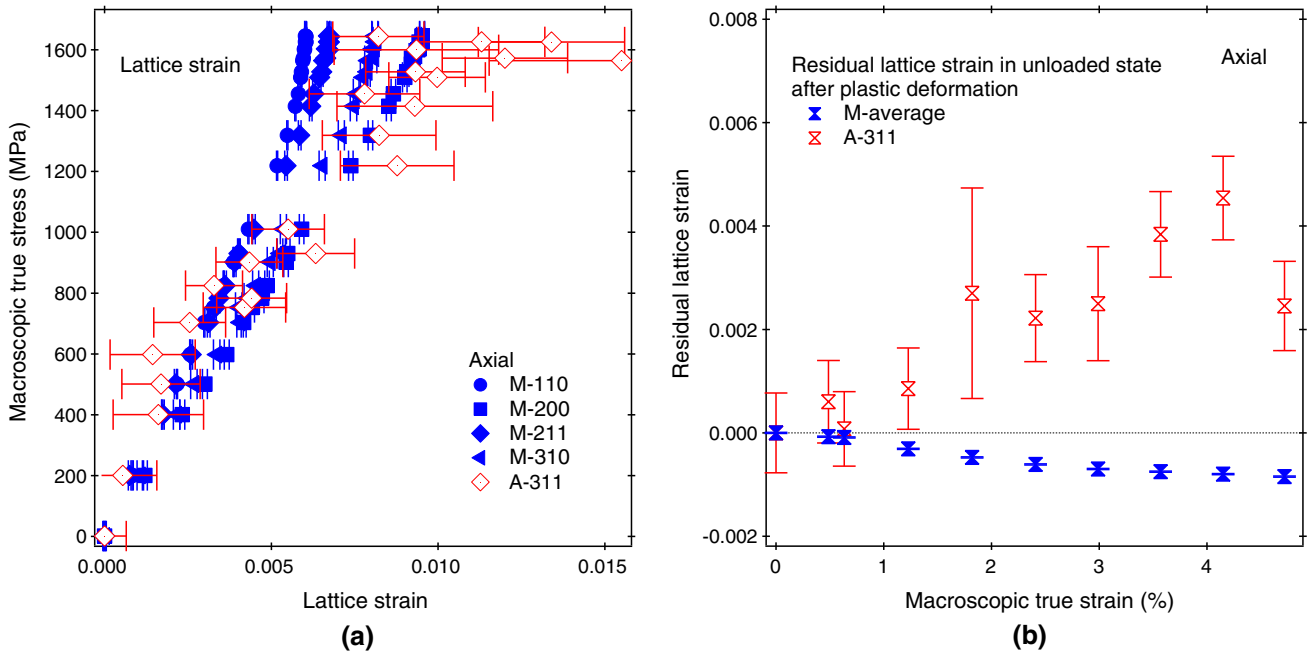


Fig. 11—(a) Lattice strains measured during tensile deformation and (b) residual lattice strains measured in unloaded states after plastic tensile deformation in the axial direction. M and A indicate martensite and retained austenite, respectively (color for online only).

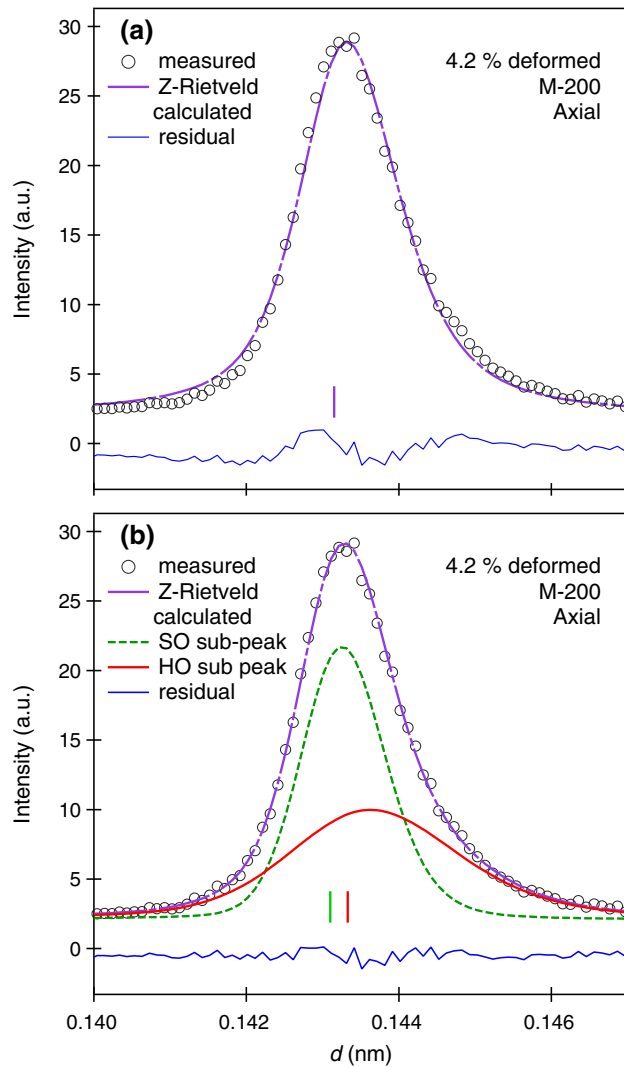


Fig. 12—Martensite-200 diffraction profiles in the 4.2 pct-deformed state in the axial direction. (a) Measured and Z-Rietveld-calculated profiles assuming a symmetrical peak profile. (b) Measured and Z-Rietveld-calculated profiles assuming a dual-packet contribution composed of two BCC structures. The sub-profiles in (b) correspond to SO and HO. The peak positions of the calculated profiles are shown with vertical bars. M indicates martensite (color for online only).

in Figure 11(b) because of the presence of  $\gamma$ . Figure 13 shows the residual component strains in the SO and the HO measured in the unloaded states after plastic tensile deformation in the axial direction. The results obtained from both the Rietveld and CMWP analyses were in good agreement within the analytical error. The residual component strains in the SO were compressive, whereas those in the HO were tensile, and their absolute values became larger with increasing macroscopic strain. This indicates that work softening occurs in the SO as opposed to work hardening in the HO. The increases in the residual component strain values in the SO and HO became small at macroscopic strain values above approximately 2.5 pct, and the increase in flow stress (Figure 1) was also small. The difference in the residual component strain at the largest macroscopic true strain was approximately 0.29 pct (570 MPa).

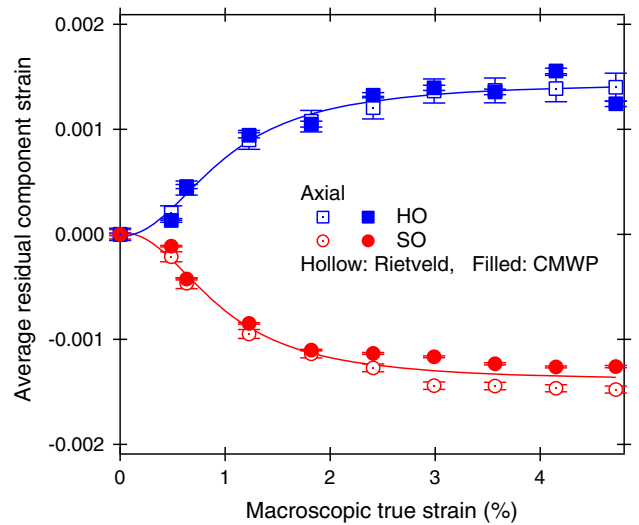


Fig. 13—Residual component strain as a function of macroscopic strain in the HO and SO analyzed using the Rietveld and CMWP methods (color for online only).

Figure 14 shows the lattice strain distribution among  $\gamma$ , SO, and HO, which was evaluated as follows. The lattice strain responses to macroscopic stress in Figure 11(a) were averaged and smooth-interpolated to determine the phase strain and phase stress of martensite. The stress balances of residual component stresses in the SO and the HO were considered to be the martensite phase stresses for the related macroscopic stresses by assuming that the Young's moduli of SO and HO were identical, and that no stress-relaxation occurred during unloading. The lattice strain distribution reflects the partitioning of load among  $\gamma$ , SO, and HO. The lattice strain of  $\gamma$  showed the largest value during macroscopic plastic tensile deformation; however, its contribution to the entire flow stress was less than 6 pct because of its small volume fraction. Therefore, the HO is considered to play the most important role in work hardening in this specimen during tensile deformation.

#### G. The $\alpha$ Coefficient in Taylor's Equation

Since the average dislocation densities in the present lath martensite steel were found to hardly change during plastic tensile deformation, the observed large work hardening was hypothesized to be related to an increase in the  $\alpha$  coefficient in Taylor's equation. The  $\alpha$  coefficients for HO ( $\alpha_{HO}$ ) and for SO ( $\alpha_{SO}$ ) for this specimen can be estimated from the macroscopic stress-strain curve and the values of  $\rho_{HO}$  and  $\rho_{SO}$  based on a composite model using the following equation:

$$\Delta\sigma = \sigma - \sigma_0 = \mu M_T b (f_{HO} \alpha_{HO} \sqrt{\rho_{HO}} + (1 - f_{HO}) \alpha_{SO} \sqrt{\rho_{SO}}). \quad [7]$$

The values of  $\sigma_0$ ,  $\mu$ ,  $M_T$ , and  $b$  used in the calculations were 350 MPa, 77.3 GPa, 2.8, and 0.248 nm, respectively. The  $\alpha_{SO}$  value at the beginning of deformation

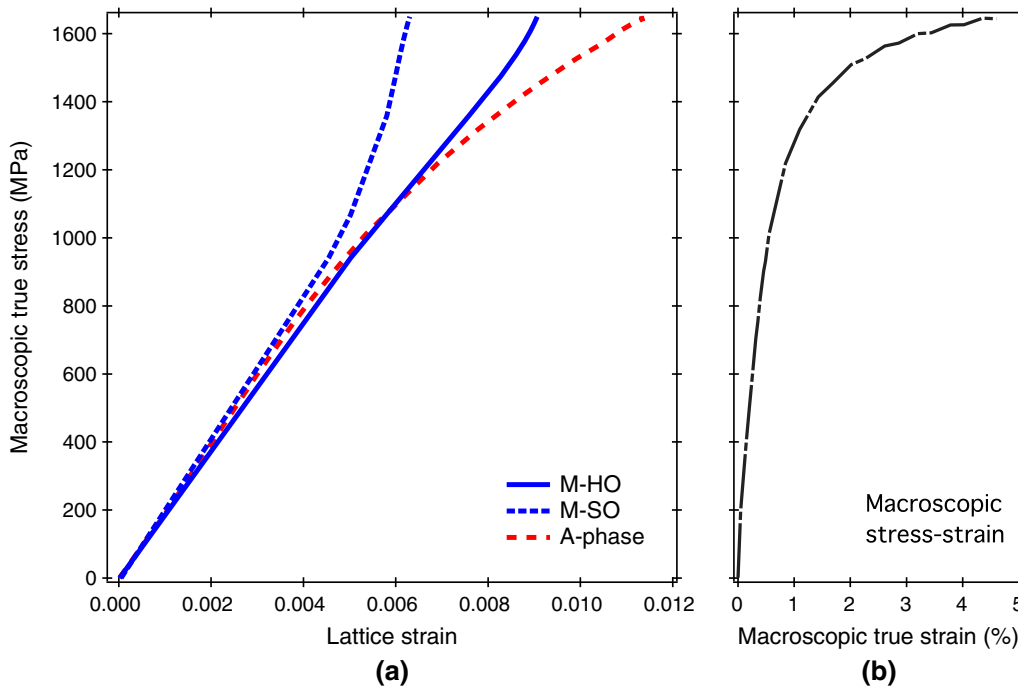


Fig. 14—(a) Lattice strain distribution during tensile deformation estimated from the lattice strains in Figure 11(a) and the residual component strains in Figure 13. M and A indicate martensite and retained austenite, respectively. (b) The relevant macroscopic stress–strain data (color for online only).

was determined to be approximately 0.18 and was fixed during further tensile deformation because of the work softening in the SO.

Figure 15 shows the calculated  $\alpha_{HO}$  values. The value of  $\alpha_{HO}$  clearly increased rapidly at the beginning of plastic deformation and then gradually varied with the progress of tensile deformation. The  $\alpha_{HO}$  value saturated at approximately 0.4, which is the value frequently used for metallic materials.<sup>[44]</sup> However, although the values of  $\alpha$  vary widely,<sup>[45,46]</sup>  $\alpha$  is considered to be constant during deformation in many studies.<sup>[4,45–47]</sup> The  $\alpha$  coefficient is determined from the angle between adjacent dislocation segments at a point where the dislocation breaks free from an obstacle.<sup>[48]</sup> In an *in situ* ND study during the tensile loading of a stainless steel, the  $\alpha$  coefficients were found to differ depending on the individual  $\langle hkl \rangle$  grain families.<sup>[36]</sup> The  $\alpha$  coefficient was large in  $\langle hkl \rangle$  grain families with larger Schmid factors, in which dislocations were arranged in longitudinal bands frequently divided by sub-boundaries, and low in the other families with smaller Schmid factors, in which the cell structure was evolved.<sup>[36]</sup>

The values of  $\Delta\sigma$  and  $M_{HO}$  are superimposed in Figure 15. Note that the vertical axis depicting  $M_{HO}$  in Figure 15 is in reverse order. Thus, in Figure 15, a rapid increase in  $\Delta\sigma$  value is proportional to a rapid decrease in  $M_{HO}$ , which is related to an increase in  $\alpha_{HO}$ . Schaffer *et al.*<sup>[49]</sup> also reported that  $M$  can be linked to  $\alpha$  in Taylor's equation of flow stress, although their results did not indicate a direct relationship. The change in  $\alpha$  with changes in dislocation arrangement during plastic tensile deformation was recently discussed in detail by Mughrabi.<sup>[50]</sup> According to Mughrabi's composite

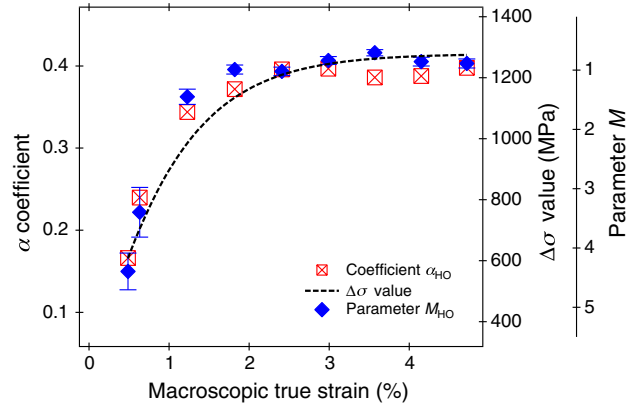


Fig. 15—Values of  $\alpha$  calculated from the dislocation densities according to Taylor's equation (Eq. [7]) and its relationships with the change in flow stress caused by dislocations and the parameter  $M$  determined from the stress–strain curve for the HO (color for online only).

model,  $\alpha$  is proportional to the square root of the cell wall volume fraction, where an increase in cell wall volume fraction increases  $\alpha$ . Hence, the decrease in  $M_{HO}$  with increasing plastic deformation suggests that the dislocations are rearranged, becoming dipole character related to constructing cell walls, and  $\alpha_{HO}$  increases as a result.

#### IV. CONCLUSIONS

*In situ* ND was performed during the tensile deformation of a lath martensite steel containing 0.22 mass

pct carbon using a high-resolution TOF neutron diffractometer. The sample showed extremely large work hardening at the beginning of plastic deformation. The results are summarized as follows.

- (1) The dislocation density of the lath martensite in the as-heat-treated state was in the order of  $10^{15}$   $m^{-2}$ . The average dislocation density obtained from CMWP analysis changed little during tensile deformation, in good agreement with the STEM observations of microstructure.
- (2) The diffraction peaks in the plastically deformed states were asymmetric, reflecting the partitioning of load, and different dislocation densities/arrangements in the two lath packets: SO, where dislocation glides are favorable, and HO, where they are unfavorable. During tensile straining, the dislocation density increased in the HO accompanied by an increase in load sharing, indicating work hardening. In contrast, the dislocation density decreased in the SO, indicating work softening. The dislocation character and arrangement varied in the HO but hardly changed in the SO. In the HO, the dislocations in the as-heat-treated state, which were mainly screw-type, became primarily edge-type and rearranged towards a dipole character related to constructing cell walls.
- (3) The HO played an important role in work hardening in the lath martensite steel during tensile deformation.
- (4) The extremely large work hardening could not be sufficiently accounted for by the increase in dislocation density; it was also necessary to consider the change in dislocation arrangement. Dislocation arrangement could be accounted for through the  $\alpha$  coefficient in Taylor's equation, which could be estimated from the variation in  $M$  determined by CMWP analysis.

#### ACKNOWLEDGMENTS

The authors acknowledge Professor Shigeo Sato of Ibaraki University for the valuable discussion. ND experiments were performed at BL19 in the Materials and Life Science Facility of J-PARC under proposals 2014I0019 and 2014P0102. Partial financial support was provided by the Japan Society for the Promotion of Science Grant-in-Aid for Scientific Research (Grant Nos. 26289264, 15H05767) and Education Commission of Hubei Province of China (Grant No. B20161203).

#### REFERENCES

1. T. Maki: *Proc. 1st Int. Symp. on Steel Sci.*, 2007, pp. 1–10.
2. S. Morito, H. Tanaka, R. Konishi, T. Furuhashi, and T. Maki: *Acta Mater.*, 2003, vol. 51, pp. 1789–99.

3. H. Kitahara, R. Ueji, N. Tsuji, and Y. Minamino: *Acta Mater.*, 2006, vol. 54, pp. 1279–88.
4. K. Nakashima, Y. Fujimura, H. Matsubayashi, T. Tsuchiyama, and S. Takaki: *Tetsu-to-Hagane*, 2007, vol. 93, pp. 459–65.
5. S. Morooka, Y. Tomota, and T. Kamiyama: *ISIJ Int.*, 2008, vol. 48, pp. 525–30.
6. G.K. Williamson and R.E. Smallman: *Philos. Mag.*, 1956, vol. 1, pp. 34–46.
7. G.I. Taylor: *Proc. R. Soc. A*, 1934, vol. 45, pp. 362–87.
8. T. Ungár, L. Li, G. Tichy, W. Pantleon, H. Choo, and P.K. Liaw: *Scr. Mater.*, 2011, vol. 64, pp. 876–79.
9. B. Hutchinson, D. Lindell, and M. Barnett: *ISIJ Int.*, 2015, vol. 55, pp. 1114–22.
10. M.R. Daymond, C.N. Tomé, and M.A.M. Bourke: *Acta Mater.*, 2000, vol. 48, pp. 553–64.
11. Y. Tomota, P. Lukas, S. Harjo, J.-H. Park, N. Tsuchida, and D. Neov: *Acta Mater.*, 2003, vol. 51, pp. 819–30.
12. Y. Tomota, H. Tokuda, Y. Adachi, M. Wakita, N. Minakawa, A. Moriai, and Y. Morii: *Acta Mater.*, 2004, vol. 52, pp. 5737–45.
13. M.R. Daymond, C. Hartig, and H. Mecking: *Acta Mater.*, 2005, vol. 53, pp. 2805–13.
14. O. Muransky, P. Sittner, J. Zrnik, and E.C. Oliver: *Acta Mater.*, 2008, vol. 56, pp. 3367–79.
15. S. Harjo, J. Abe, K. Aizawa, W. Gong and T. Iwahashi: *JPS Conf. Proc.*, 2014, vol. 1, 014017.
16. S. Morooka, T. Tsuchiyama, S. Harjo, and K. Aizawa: *CAM-P-ISIJ*, 2014, vol. 168, p. 866.
17. T. Ungár, S. Harjo, T. Kawasaki, Y. Tomota, G. Ribarik, and Z. Shi: *Metall. Mater. Trans. A*, 2016, vol. 48A, pp. 159–67.
18. H. Mughrabi, T. Ungár, W. Kienle, and M. Wilkens: *Philos. Mag. A*, 1986, vol. 53, pp. 793–813.
19. B. Jakobsen, H.F. Poulsen, U. Lienert, J. Almer, S.D. Shastri, H.O. Sørensen, C. Gundlach, and W. Pantleon: *Science*, 2006, vol. 312, pp. 889–92.
20. T. Ungár, J. Gubicza, G. Ribarik, and A. Borbely: *J. Appl. Cryst.*, 2001, vol. 34, pp. 298–310.
21. G. Ribarik and T. Ungár: *Mater. Sci. Eng. A*, 2010, vol. 528, pp. 112–21.
22. Z. Shi, K. Liu, M. Wang, J. Shi, H. Dong, J. Pu, B. Chi, Y. Zhang, and L. Jian: *Met. Mater. Int.*, 2012, vol. 18, pp. 317–20.
23. S. Harjo, T. Ito, K. Aizawa, H. Arima, J. Abe, A. Moriai, T. Iwahashi, and T. Kamiyama: *Mater. Sci. Forum*, 2011, vol. 681, pp. 443–48.
24. R. Oishi, M. Yonemura, Y. Nishimaki, S. Torii, A. Hoshikawa, T. Ishigaki, T. Morishima, K. Mori, and T. Kamiyama: *Nucl. Instrum. Methods A*, 2009, vol. 600, pp. 94–96.
25. K. Iakoubovskii, K. Mitsuishi and K. Furuya: *Nanotechnology*, 2008, vol. 19, 155705.
26. O.D. Sherby, J. Wadsworth, D.R. Lesuer, and C.K. Syn: *Mater. Trans.*, 2008, vol. 49, pp. 2016–27.
27. Y. Tomota, H. Tokuda, S. Torii, and T. Kamiyama: *Mater. Sci. Eng. A*, 2006, vol. 434, pp. 82–87.
28. L.D. Landau and E.M. Lifshitz: *Theory of Elasticity*, 1 Englishst ed., Pergamon Press, London, 1959, pp. 1–42.
29. T.H. Courtney: *Mechanical Behavior of Materials*, 2nd ed., Waveland Press Inc., Long Grove, 1990, pp. 44–84.
30. S.A. Kim and W.L. Johnson: *Mater. Sci. Eng. A*, 2007, vols. 452–453, pp. 633–39.
31. T. Ungár and A. Borbely: *Appl. Phys. Lett.*, 1996, vol. 69, pp. 3173–75.
32. T. Ungár and G. Tichy: *Phys. Stat. Sol. (a)*, 1999, vol. 171, pp. 425–34.
33. T. Ungár, I. Dragomir, Á. Révész, and A. Borbely: *J. Appl. Cryst.*, 1999, vol. 32, pp. 992–1002.
34. A. Shibata, S. Morito, T. Furuhashi, and T. Maki: *Acta Mater.*, 2009, vol. 57, pp. 483–92.
35. S. Morito, J. Nishikawa, and T. Maki: *ISIJ Int.*, 2003, vol. 43, pp. 1475–77.
36. T. Ungár, A.D. Stoica, G. Tichy, and X.L. Wang: *Acta Mater.*, 2014, vol. 66, pp. 251–61.
37. X. Huang, S. Morito, N. Hansen, and T. Maki: *Metall. Mater. Trans. A*, 2012, vol. 43A, pp. 3517–31.
38. V. Vitek: *Philos. Mag.*, 2004, vol. 84, pp. 415–28.
39. U. Essmann and H. Mughrabi: *Philos. Mag. A*, 1979, vol. 40, pp. 731–56.



40. D. Akama, T. Tsuchiyama, and S. Takaki: *ISIJ Int.*, 2016, vol. 56, pp. 1675–80.
41. S. Morito, T. Ohba, A.K. Das, T. Hayashi, and M. Yoshida: *ISIJ Int.*, 2013, vol. 53, pp. 2226–32.
42. D.A. Hughes and N. Hansen: *Acta Mater.*, 2000, vol. 48, pp. 2985–3004.
43. J. Stráská, M. Janeček, J. Gubicza, T. Krajňák, E.Y. Yoon, and H.S. Kim: *Mater. Sci. Eng. A*, 2015, vol. 625, pp. 98–106.
44. H. Mughrabi: *Mater. Sci. Eng.*, 1987, vol. 85, pp. 15–35.
45. N. Hansen and X. Huang: *Acta Mater.*, 1998, vol. 46, pp. 1827–36.
46. T. Waitz, H.P. Karnthaler and R.Z. Valiev: in Zehetbauer, M.J., Valiev, R.Z. (Eds.), *Nanomaterials by Severe Plastic Deformation*, 2004, Wiley-VCH, New York, pp. 337–50.
47. J.A. El-Awady: *Nat. Commun.*, 2015, vol. 6, p. 5926.
48. K. Hanson and J.W. Morris, Jr: *J. Appl. Phys.*, 1975, vol. 46, pp. 983–90.
49. E. Schafler, K. Simon, S. Bernstorff, P. Hanák, G. Tichy, T. Ungár, and M.J. Zehetbauer: *Acta Mater.*, 2005, vol. 53, pp. 315–22.
50. H. Mughrabi: *Curr. Opin. Solid State Mater. Sci.*, 2016, vol. 20, pp. 411–20.